RESEARCH ARTICLE

NANO · MICRO small
www.small-journal.com

Rational Design of Improved Ru Containing Fe-Based Metal-Organic Framework (MOF) Photoanode for Artificial Photosynthesis

*Jully Patel, Gabriel Bury, and Yulia Pushkar**

Metal-Organic Frameworks (MOFs) recently emerged as a new platform for the realization of integrated devices for artificial photosynthesis. However, there remain few demonstrations of rational tuning of such devices for improved performance. Here, a fast molecular water oxidation catalyst working via water nucleophilic attack is integrated into the MOF MIL-142, wherein Fe_3O nodes absorb visible light, leading to charge separation. Materials are characterized by a range of structural and spectroscopic techniques. New, $[Ru(tpy)(Qc)(H_2O)]^+$ (tpy = 2,2′:6′,2″-terpyridine and Qc = 8-quinolinecarboxylate)-doped Fe MIL-142 achieved a high photocurrent (1.6×10^{-3} A·cm^{-2}) in photo-electrocatalytic water splitting at pH = 1. Unassisted photocatalytic H_2 evolution is also reported with Pt as the co-catalyst (4.8 μmol g^{-1} min^{-1}). The high activity of this new system enables hydrogen gas capture from an easy-to-manufacture, scaled-up prototype utilizing MOF deposited on FTO glass as a photoanode. These findings provide insights for the development of MOF-based light-driven water-splitting assemblies utilizing a minimal amount of precious metals and Fe-based photosensitizers.

1. Introduction

Energy is vital but is primarily sourced from depleting, polluting, and non-renewable fossil fuels, necessitating a shift to cleaner sources.[1] Harvesting sunlight through artificial photosynthesis provides carbon-free, eco-friendly energy.[2–5] In recent years, water oxidation catalysts (WOCs) have been developed based on ruthenium,[6–10] manganese,[11–15] iron,[16–19] and iridium.[20–23] To utilize the chemical reactivity of these catalysts, one must integrate them into more complex assemblies for artificial photosynthesis. One approach is to create dye-synthesized, photo-electrochemical cells.[24–27] Such cells were reported with both a catalyst and a dye adsorbed onto the surfaces of semiconductor materials, such as TiO_2.[28–30] One weakness of these molecular assemblies is the desorption of the catalysts and dyes from the surface due to the failure of molecular linkers such as carboxylate and phosphonate groups.[31]

Very recently, researchers incorporated molecular WOCs into metal-organic frameworks (MOF)s,[32–37] which have the distinct advantages of large surface areas, high synthetic tunability allowing to introduce unique chemical functionalities, excellent stability, and in some cases, photocatalytic properties . Furthermore, incorporating WOCs into MOF eliminates bimolecular degradation pathways, common in solutions of these catalysts. Successful incorporation eases the separation of WOC-functionalized MOFs from solution for catalyst characterization following the water oxidation reaction.[38] An early report featured an Ir molecular WOC in a Zr-based MOF, where the channel size was increased due to the use of elongated bpy-dc and ppy-dc -containing dicarboxylate ligands (bpy-dc = dibenzoate-substituted 2,2′-bipyridine, ppy-dc = dibenzoate-substituted 2-phenylpyridine), **Figure 1**.[38] The well-studied [Ru(tpy)(bpy)] (bpy = 2,2′-Bipyridine and tpy = 2,2′:6′,2″-terpyridine) catalyst was incorporated into the UiO-67 MOF and was shown to be active in chemical and electrochemical water oxidation catalysis.[33] Using this strategy, other WOCs functionalized with carboxylic acid groups were incorporated into the UiO-67 and NU-1000 (NU = Northwestern University) frameworks for electrocatalytic water oxidation, Figure 1.[39,40] Using the same UiO-67 framework, our group reported a MOF with *cis*-$[Ru(bpy)(dcbpy)(H_2O)_2]^{2+}$ (dcbpy = 2,2′-bipyridine-5,5′-dicarboxylic acid); the incorporation of this catalyst within the UiO-67 MOF framework increased electrocatalytic activity.[41] In 2021, Wang et al. reported the incorporation of Ir complexes in UiO-67, but the small open channel of this MOF prohibited access of hydrated Ce^{4+} used to drive water oxidation catalysis. Thus, only WOCs on the surface of these MOF particles participated in water oxidation, leaving intact the Ir*Cp complexes inside while they typically undergo oxidative decomposition during the water oxidation.[38,42–44] In addition to these

J. Patel, G. Bury, Y. Pushkar
Department of Physics and Astronomy
Purdue University
West Lafayette, IN 47907, USA
E-mail: ypushkar@purdue.edu

The ORCID identification number(s) for the author(s) of this article can be found under https://doi.org/10.1002/smll.202310106

DOI: 10.1002/smll.202310106

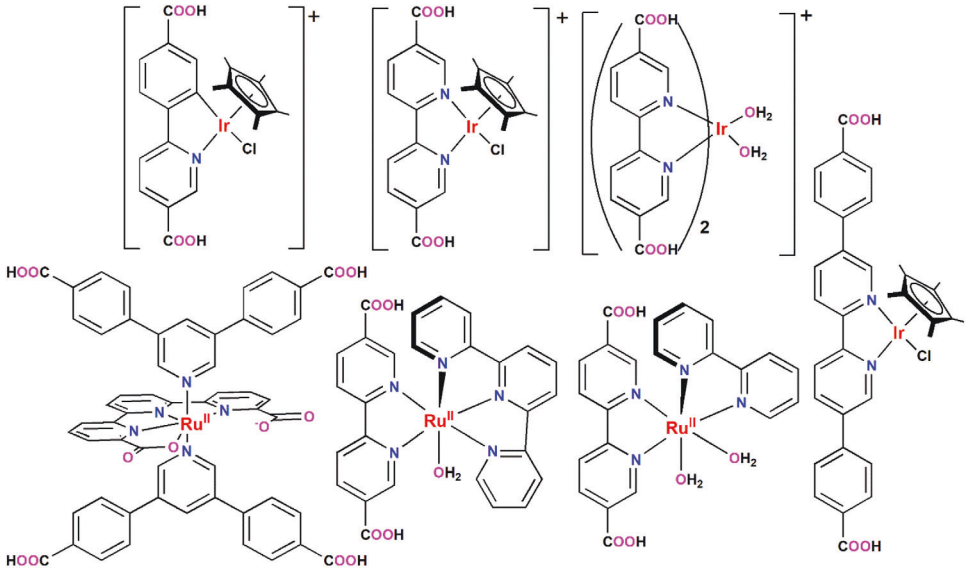

Figure 1. Structure of mononuclear WOCs incorporated in UiO-67, NU-1000, and MIL-126 MOFs.[38–40,43,52,58]

issues, enumerated above MOF composites lack light-absorption properties in the visible energy range.

Fe-based MOFs with Fe_3O nodes, including MIL-101(Fe), MIL-126(Fe), MIL-100(Fe), MIL-88(Fe), and MIL-53(Fe), can catalyze visible-light-driven water oxidation when supplied with an electron acceptor.[35,45,46] The photocatalytic abilities of certain MOFs – like MIL-100(Fe), MOF-5, UiO-66-NH_2, UiO-66, and ZIF-8 – improved by adding active components: Pt, Ni, NiO, Au, and TiO_2, to the interior/surface of porous MOFs.[46–51] The resulting enhanced photocatalysts evolved hydrogen at rates from 30.22 to 109 μmol $g^{-1}h^{-1}$, but all required sacrificial electron acceptors. We found that Fe-based MIL-126 enables photo-electrocatalytic water oxidation at pH = 1, when combined with a Ru-based WOC ($[Ru(bpy)(dcbpy)(H_2O)_2]^{2+}$), achieving a photocurrent of 2×10^{-4} A·cm^{-2}.[52]

The development of WOCs for catalytic water oxidation with higher catalytic rates and lower overpotentials is desired yet challenging. Radical coupling (RC) mechanisms allow for the fastest O—O bond formation,[53] but such mechanisms are difficult to engineer into the device architecture. RC mechanisms were demonstrated in catalyst solutions with bi-molecular deactivation pathways resulting in dimer and trimer formation, as well as in single-metal complexes with N-oxide ligand in a non-cyclical, non-catalytic manner.[54] RC was also proposed for the action of the Mn_4Ca oxygen-evolving complex of Photosystem II[55] and was found to be consistent with a time-resolved spectroscopic analysis of the OEC.[56] Due to the difficulty of engineering the molecular RC WOCs, we focused on the improvement of WNA catalyst activities and identification of the true molecular catalysts via monitoring of the lag phases, Tables S12 (Supporting Information). Hoque et al. reported a set of Ru-based WOCs (*cis*- and *trans*-$[Ru(tpy)(Qc)(H_2O)]^{2+}$),[57] noting *trans*-isomers were more active.

Here, we further investigated the *trans*-[Ru(NNN)(Qc)X] scaffold sensitivity to electron-donating and electron-withdrawing groups by preparation of the $[Ru(R\text{-}tpy)(Qc)(H_2O)]^+$ (where R = H (**1**), Cl (**2**), and EtO (**3**), EtO-tpy = 4-ethoxy-2,2′:6′,2″-terpyridine, Qc = 8-quinoline carboxylate, **Figure 2**a) series. We concluded that the parent *trans*-$[Ru(tpy)(Qc)(H_2O)]^+$ compound, **1**, is the most active and selected it for incorporation into the newly designed MOF. **1** was incorporated into the MIL-142 Fe MOF with the H_3-Tpy linker (H_3-Tpy = 4′-(4-carboxyphenyl)-[2,2′:6′,2″-terpyridine]−5,5′″-dicarboxylic acid) used for catalyst integration and with BDC (BDC = terephthalic acid) and BTB (BTB = 1,3,5-Tris(4-carboxyphenyl)benzene) linkers (Figure 2b–d).[59,60] Despite the reported sensitivity of the iron-based nodes to the acidic conditions,[59,60] we were able to stabilize these materials on an FTO glass electrode for prolonged photo-electrocatalytic water oxidation at pH = 1 using a proton-conductive Nafion membrane. MOF materials were also analyzed with X-ray diffraction (XRD), scanning electron microscopy (SEM), Fourier-transform infrared spectroscopy (FT-IR), electron paramagnetic resonance (EPR), and electric conductivity measurements.

2. Results and Discussion

2.1. Synthesis and Characterization of Molecular Catalysts

The ligand H_3-TPY, [Ru(p-cymene)(Qc)Cl], *trans*-$[Ru^{II}(R\text{-}tpy)(Qc)Cl]$, *trans*-$[Ru^{II}(R\text{-}tpy)(Qc)(H_2O)](PF_6)$, and $[Ru(H_3\text{-}Tpy)(Qc)Cl]$ were prepared by using reported procedures (Scheme S1, Supporting Information)[52,57,61] and characterized by ^{1}H NMR and ESI mass spectroscopy (Figures S1–S8, Supporting Information). UV–vis of **WOCs 1**, **2**, and **3** appear in Figure S9 (Supporting Information). Peaks at 549 nm and 486 nm can be assigned to the Metal-to-Ligand charge transfer (MLCT) in **WOC 1** and **3**, respectively. Peaks at 551 and 508 nm are assigned to MLCT in **WOC 2**.

The complexes' electrochemical behavior was determined with 0.5 mM solutions of the catalyst in 0.1 M HNO_3 (Figure S10a, Supporting Information). Using cyclic voltammetry (CV), the

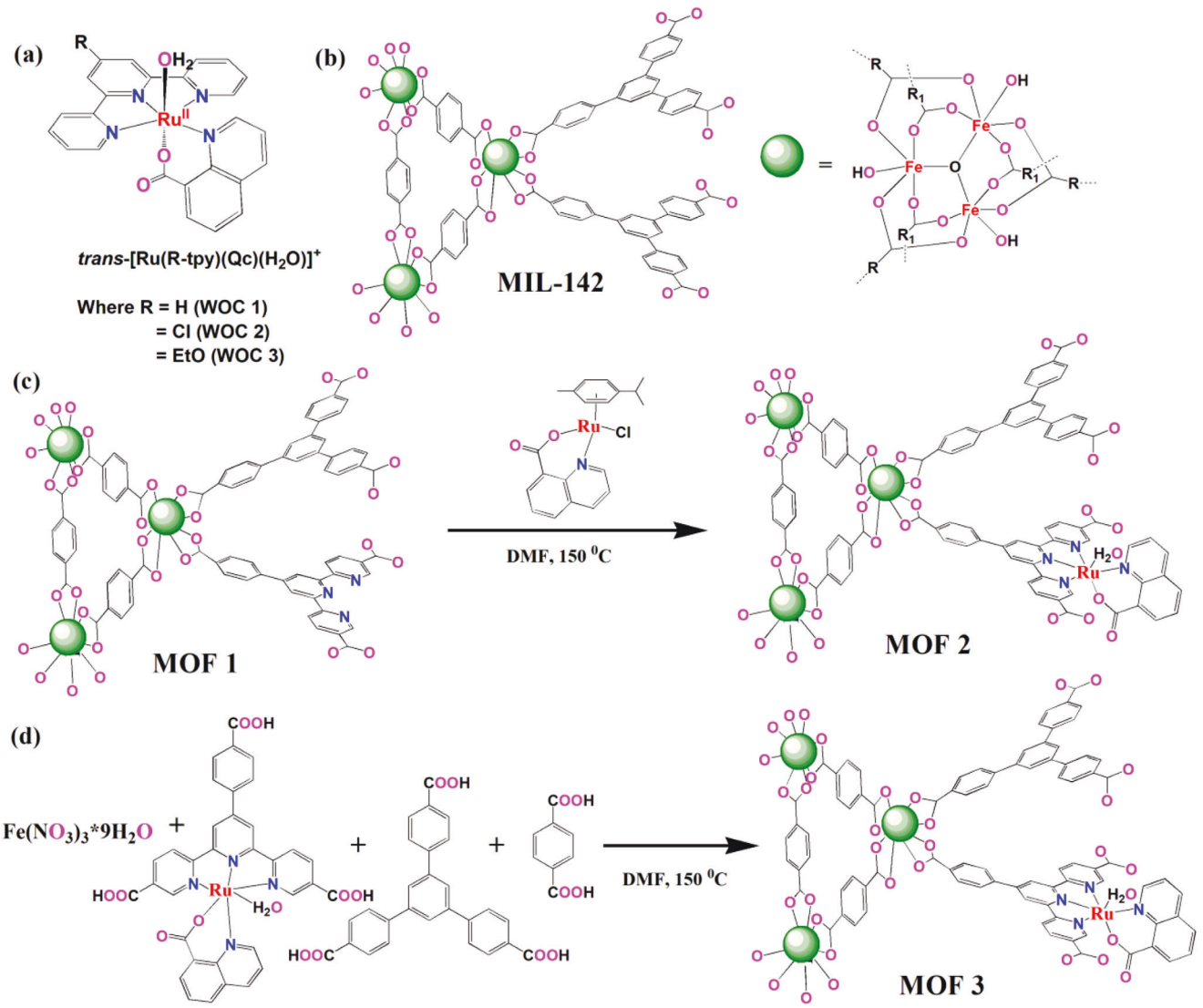

Figure 2. a) Structures of *trans*-[Ru^{II}(R-tpy)(Qc)(H_2O)]$^+$ (**WOCs**), b) structure of MIL-142 MOF c) synthetic scheme of **MOF 2** showing the integration of the precursor [Ru(p-cymene)(Qc)(Cl)], and d) synthetic scheme of **MOF 3** showing the integration of the *trans*-[Ru(H_3-Tpy)(Qc)(H_2O)]$^+$ catalytic unit.

Ru^{II}/Ru^{III} reversible redox couple was observed at 0.64 V, 0.61 V, and 0.54 V versus NHE for **WOCs 1**, **2**, and **3**, respectively. The redox couples of **WOC 1** (Ru^{II}/Ru^{III} at 0.63 V, Ru^{III}/Ru^{IV} at 1.16 V, and Ru^{IV}/Ru^{V} at 1.55 V versus NHE) agree with the values reported by Hoque.[57] Redox waves at higher potentials: 1.16 V and 1.55 V versus NHE for **WOC 1**, 1.24 V and 1.65 V for **WOC 2**, and 0.99 V and 1.53 V versus NHE for **WOC 3** (Figure S10a, Supporting Information) are assigned to Ru^{III}/Ru^{IV} and Ru^{IV}/Ru^{V}. EPR spectroscopy did not observe Ru^{V} in fast-frozen samples oxidized by ceric ammonium nitrate (CAN), see description below and Figure S18 (Supporting Information). The onset of catalytic current was detected at 1.37 V, 1.55 V, and 1.52 V versus NHE for **WOCs 1**, **2**, and **3** respectively, by extrapolation of tangents to the rising current indicating electrocatalytic water oxidation (Figure S10b, Supporting Information). **WOC 1** demonstrated lower onset potential and higher electrocatalytic current, indicating superior electrocatalytic activity.

DFT calculations[62] characterize proposed catalytic intermediates of **WOCs 1**, **2**, and **3**. Experimental redox potentials are compared with DFT-predicted ones and alternative PCET (proton-coupled electron transfer) reactions are considered, Table S2 (Supporting Information). Note, that calculations are done for pH = 0. For the first oxidation, we can see that one-electron oxidation (electron transfer, ET) and one-electron PCET are similar energetically, with one-electron PCET lower in energy. This shows that the carboxylic group *trans* to water increases the acidity of the water ligand. Interestingly, one-electron PCET predicts the lowest potential for **WOC 1**; both **WOC 2** and **3** are predicted to have higher energies. For the second oxidation step, one-electron PCET is also the most favorable and should result in the formation of Ru^{IV} = O intermediate. However, this intermediate can only convert into Ru^{V} = O state via ET, resulting in a high oxidation potential, Table S2 (Supporting Information). Considering that Ru^{IV} = O and Ru^{IV}-OH are not too dissimilar energetically

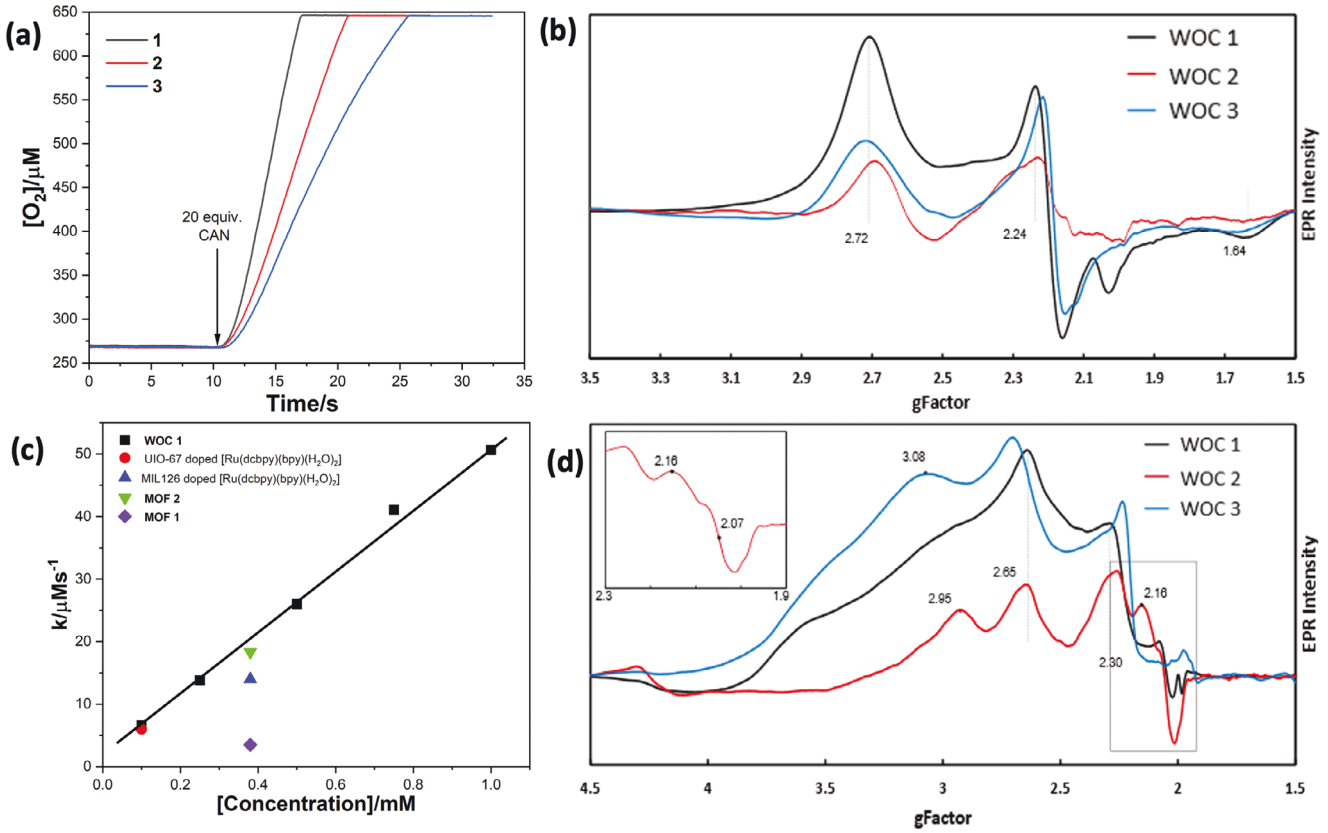

Figure 3. a) Comparison of O_2 evolution for **WOCs 1**, **2,** and **3** (0.5 mM) in 0.1 M HNO_3 with 20 equiv. of CAN added at t = 11 sec, b) EPR spectra of **WOC 1, WOC 2,** and **WOC 3** in 0.1 M HNO_3 after addition of 1equiv. CAN, c) Comparison of O_2 evolution activity of different MOFs with **WOC 1**, and d) EPR spectra of **WOC 1, WOC 2,** and **WOC 3** in 0.1 M HNO_3 after addition of 20 equiv. CAN.

(difference <0.5 eV), we propose a mixture of such species exists, and Ru^{IV}-OH to Ru^{V} = O PCET facilitates water oxidation catalysis. DFT results suggest that **WOC 3** has the most stabilized Ru^{V} = O state, as it can be achieved at the lowest potential.

2.2. Catalytic O_2 Evolution Using Molecular Catalysts

Catalytic water oxidation was performed (0.1 M HNO_3) using **WOCs 1**, **2**, and **3** as catalysts and CAN as oxidant. A Clark electrode recorded molar O_2 evolution in aerobic conditions. To determine O_2 evolution rate, the reaction was performed with varying catalyst concentrations (0.25 mM to 1.0 mM) and constant concentration of CAN (20 equiv.). O_2 evolution increased with increasing catalyst concentration (**Figure 3**a; Figures S12a, S13a, and S14a, Supporting Information). The kinetics of O_2 evolution, determined by initial rates shown in Figures S15a, S16a, and S17a (Supporting Information), was first-order with respect to catalyst concentration for all three **WOCs** (k^{CAN}_{obs} = 48.6 μM s^{-1}, 40.9 μM s^{-1} and 29.7 μM s^{-1} for **WOC 1**, **2**, and **3**, respectively, k^{CAN}_{obs} is the O_2 evolution rate at constant CAN concentration; see Figures S15b, S16b, and S17b (Supporting Information). To evaluate oxidant effect, we kept the concentration of three WOCs constant at 0.5 mM and varied the CAN concentration from 10 mM to 40 mM (Figures S12b, S13b, and S14b, Supporting Information) during O_2 evolution. Rate of O_2 evolution was also determined to be 1st-order with respect to the CAN concentration (k^{Ru}_{obs} = 1.12 μM s^{-1}, 0.73 μM s^{-1}, and 0.49 μM s^{-1} for **WOC 1**, **2**, and **3**, respectively (Figures S15c,d, S16c,d, and S17c,d, Supporting Information). The negatively charged QC ligand improves catalytic activity and eliminates the lag phase in chemically driven water oxidation (Table S1, Supporting Information). **WOC 1** is the most active catalyst for water oxidation compared to the others reported working via WNA mechanism (Tables S11, S3, and Figure S11, Supporting Information).

Cryogenic EPR spectroscopy determined the paramagnetic properties of intermediates involved in the catalytic cycle of **WOCs 1**, **2**, and **3**. The initial states of catalysts are diamagnetic, containing the low-spin Ru^{II} state (S = 0). All catalysts were oxidized with the addition of varying equivalents of CAN and were quickly frozen (<30s). The spectra of each catalyst with the addition of 1 and 20 equiv. of CAN are shown in Figure 3b,d. For all catalysts, one-electron oxidation results in a well-characterized S = ½ feature, consistent with the formation of a Ru^{III} intermediate. Previously, we showed that substitution of the EtO-tpy ligand results in a g-tensor with greater anisotropy compared to the $[Ru(tpy)(bpy)(H_2O)]^{3+}$ and the $[Ru(tpy)(4\text{-pic})_2(H_2O)]^{3+}$ catalysts.[7] Note that g-tensors reflect the non-isotropic nature of unpaired electrons in the sample, wherein spin-orbit coupling from atoms shifts the g factor away from 2 (approximately the g-factor of the free electron), while local electrostatic fields may shift orbital energy levels, resulting in anisotropies described by

a g-tensor. These new data do not immediately reinforce this trend; comparisons of EPR spectra of both catalysts oxidized with 1 equiv. of CAN (Figure 3b) indicate very similar degrees of anisotropy, as evidenced by the similar g-tensors for the S = ½ signal: **WOC 1: (**2.72, 2.21, 1.64), **WOC 3**: (2.73, 2.21, 1.66). The EPR spectra are rhombic ($g_{xx} \neq g_{yy} \neq g_{zz}$). This is unsurprising due to the asymmetries of the QC ligand and the EtO- ligand in **WOC 3**. **WOC 2** oxidized by 1 equiv. CAN reveal a similar S = ½ feature with slightly shifted g_{xx}: **WOC 2-** (2.70, 2.21, g_{zz} unresolved).

To observe if the negatively charged QC ligand might stabilize the Ru^{V} oxidation state – easily identifiable due to unique Ru^{V} EPR characteristics, Table S4 (Supporting Information) – we measured EPR spectra of the three catalysts oxidized with an excess (20 equiv.) of CAN, Figure 3d. Previously, we reported similar measurements for Ru WOCs with neutral polypyridine ligands, where oxidation with 20 equiv. of CAN resulted in the elimination of ≈90% of EPR intensity.[63,64] This was interpreted as the predominant formation of the diamagnetic, EPR-silent $Ru^{IV} = O$ state. Here, we see that oxidation with excess CAN does not resemble earlier results, and the significant presence of EPR-active species remains with g-tensors most consistent with assignment to Ru^{III}, with possibly a modified ligand environment. Our prior work considered $[Ru(EtO\text{-}tpy)(pic)_2(H_2O)]^{2+}$ WOC oxidized with excess (20 equiv.) of CAN and reported a novel EPR feature with g_{xx} = 2.17, g_{yy} = 2.07.[7] Interestingly, a similar feature is observed for **WOC 2** oxidized with excess CAN, Figure 3d, **insert**. Prior analysis suggested that this feature could be characteristic of peroxide or superoxide formation; both possible assignments are late reaction intermediates in a catalytic cycle and are plausible in the presence of excess oxidant. Despite the use of excess oxidant, we did not observe the spectroscopic signatures of Ru^{V} for any catalyst; notably absent is the g_{zz}≈1.9 feature, characteristic of $Ru^{V} = O$ formation. This may be due to the high reactivity of the purported high-valent Ru^{V} species. $Ru^{V} = O$ groups may only briefly form prior to O—O bond formation via a WNA process (the oxygen evolution rates are 1st-order with catalyst). Please note that due to the overwhelming intensity of paramagnetic iron signals in EPR, no spectral signatures of Ru centers incorporated into MOFs may be discussed; see Figure S18 (Supporting Information).

In our previous study, we reported $[Ru(R\text{-}tpy)(pic)_2(H_2O)]^{2+}$, (where pic = 4-picoline) as a catalyst for water oxidation by simple electronic modification of the backbone of the catalyst. The addition of a single electron-donating group (EtO-) to tpy ligand increased the catalyst's activity by at least a factor of two,[7] while in the $[Ru(R\text{-}tpy)(bpy)(H_2O)]^{2+}$ same modification resulted in an order of magnitude increase in the activity.[64,65] Here, we expanded the series of *trans*-$[Ru(R\text{-}tpy)(Qc)(H_2O)_2]^{2+}$ (where R = H (**1**), Cl (**2**), and EtO-tpy (**3**)) by introducing the electron-donating and withdrawing groups but activity was best for **WOC 1** with unmodified ligand. Overall, the addition of a negatively charged QC ligand not only improved the catalytic activity but also eliminated the lag phase in chemically driven water oxidation (Table S1, Supporting Information), suggesting that the starting Ru complex is a true catalyst. **WOC 1** is currently the most active catalyst for water oxidation as compared to the other reported catalysts working via WNA mechanism; see Table S3 (Supporting Information) and Figure 3a; Figure S11 (Supporting Information). Figures S15b, S16b, and S17b (Supporting Information) suggest that these complexes show first-order kinetics for chemical water oxidation.

2.3. Synthesis and Characterization of MOFs

Following the confirmation of high catalytic activity, we endeavored to incorporate **WOC 1** into the MIL-142 Fe MOF to achieve light-induced water oxidation catalysis. We modified the tpy ligand, resulting in H_3Tpy with three COOH groups capable of coordinating with Fe_3O nodes in the MOF, Figure 2b. **MOF 1** containing ≈10% of H_3Tpy ligand in MIL-142 framework was prepared. Two approaches to introducing **WOC 1** into the MOF were explored: using precursor Ru(p-cymene)(Qc)(Cl) to react with H_3Tpy fragments of **MOF 1** (Figure 2c), or forming the MIL-142 with pre-synthesized *trans*-$[Ru(H_3\text{-}Tpy)(Qc)(H_2O)]^{+}$ catalyst (Figure 2d). Both methods resulted in Ru-doped MIL-142 MOFs (**MOF 2** and **3**), enhancing the catalytic activity of the composite MOF. The crystalline structure of products in both synthetic approaches producing **MOF 2** and **3** matches the expected pattern of MIL-142 (**Figure** 4a). The 2.5 nm-diameter pores of MIL-142[66] allow diffusion of Ru(Qc)(p-cymene)Cl with maximum dimension – distance between the most distal hydrogens of the QC and p-cymene ligands − 13Å. Thus, pre-catalyst might be delivered into the crystals of the MIL-142 MOF during the post-synthetic treatment. The same work reported theoretical pore densities of ≈0.7 cm^3g^{-1},[67] suggesting an approximate one-to-one ratio of pores to the number of ruthenium complexes introduced via post-synthetic modification or direct synthesis. Scanning electron microscopic (SEM) images of MOFs show that MIL-142, **MOF 1**, **2**, and **3** with Fe MIL-142 topology form octahedral structures (Figure 4b,d; Figure S20a,b, Supporting Information). The Fe/Ru ratio was assessed from inductively coupled plasma mass spectrometry (ICP-MS) measurements. The content of $[Ru(H_3\text{-}tpy)(Qc)(H_2O)]^{+}$ within the as-prepared **MOF 3** is measured at 0.16 µmol/1 mg of the MOF, corresponding to ≈1:1 molar ratio of the Ru complex to the H_3-tpy linker of **MOF 3**. **MOF 2** and **3** demonstrated a Fe/Ru ratio of 9.14 and 9.29, indicating that the Ru catalyst is distributed on the exterior and within the crystalline structure. The oxidation state of Ru was assessed to be Ru^{II} using XPS, Figure S21a–c. In **MOF 2**, the XPS peaks at 280.9 eV and 286.4 eV were assigned to Ru $3d_{5/2}$ and Ru $3d_{3/2}$, while for the RuO_2 $3d_{5/2}$ peaks around 281.6-282.6 are expected.[68–70] FTIR spectra of the MOFs reveal carbonyl group vibrations in the 1200–1650 cm^{-1} range, alongside aromatic bands at 800–1200 cm^{-1} for BDC, BTB, and H_3Tpy (Figure S21d, Supporting Information). The similarity of the FTIR spectra of the MOFs before and after doping with Ru indicates that MOF crystalline structure remains unaltered upon Ru doping. All MOFs' conductivity was measured with and without light using our custom-made setup (Figure S22, Table S5, Supporting Information).[52]

The UV-visible diffuse reflectance spectra demonstrate that the absorbance extends into the visible light region for all MOFs and its intensity correlates with the presence of Ru catalyst (Figure S23, Supporting Information). The bandgap of the MOFs was determined by transforming the UV-visible diffuse reflectance spectra to Kubelka-Munk plots. The bandgap for MIL-142 is 2.45 eV, **MOF 1** is 2.5 eV, and both **MOF 2** and **3** show

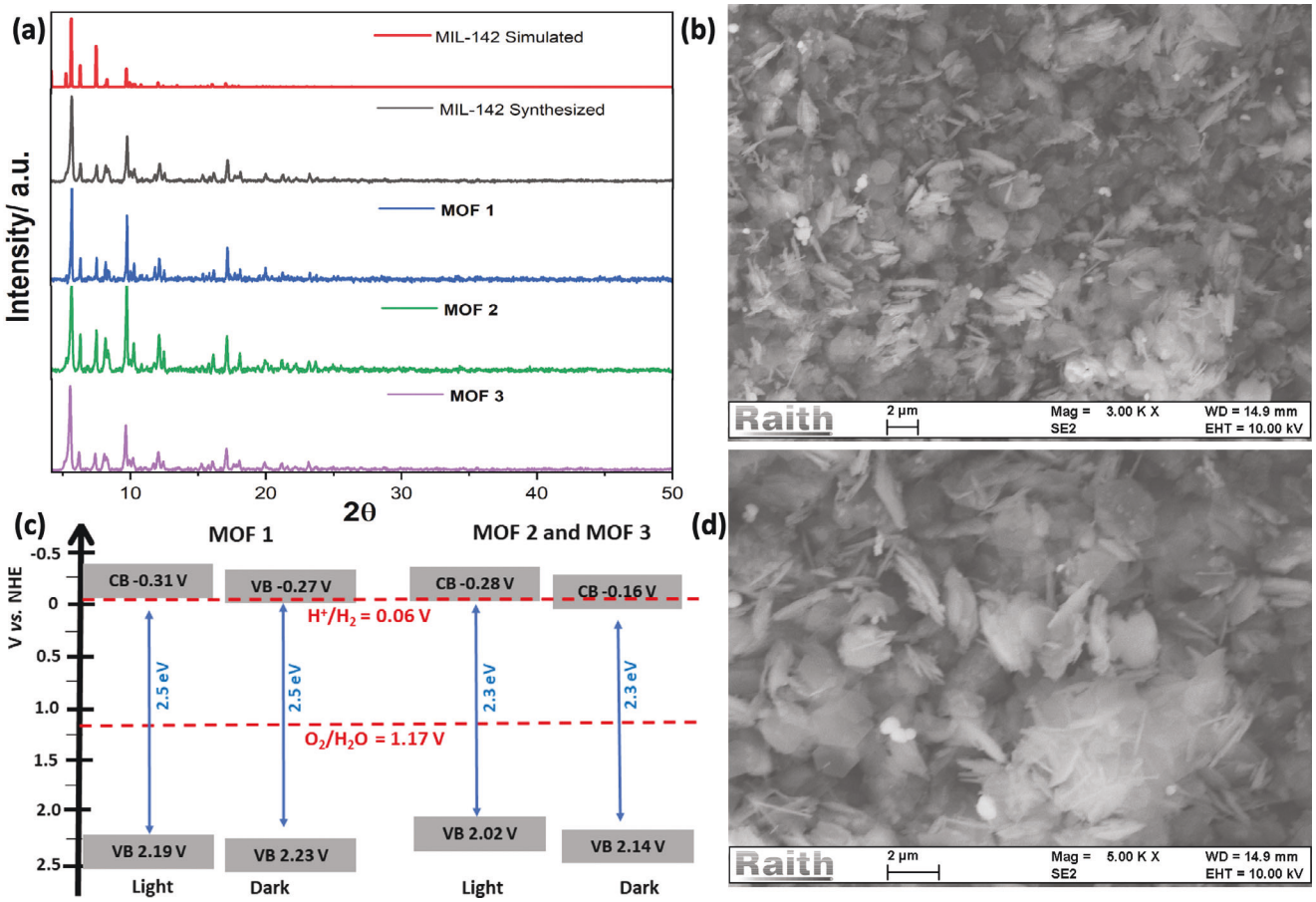

Figure 4. a) Powder X-ray diffraction (PXRD) pattern of the MOFs: MIL-142 simulated (red), MIL-142 synthesized (black), **MOF 1** (blue), **MOF 2** (green), and **MOF 3** (purple), SEM images of the **MOF 2** b) and **MOF 3** d), c) Band position of **MOF 1** (left) and **MOF 2**, **MOF 3** (right).

the same band gap of 2.31 eV (Figure S24, Supporting Information) which is comparable with the bandgap of the reported Fe-based MOFs (2.3 eV for Fe MIL-126).[52] Similar to a prior report,[59] we have not observed a direct correlation between absorbance and photoelectrochemical water splitting performance of the **MOFs 1**, **2**, and **3**, suggesting that not all "colored" system components are photosensitizing for water oxidation. We expect Fe_3O nodes to be an active photosensitizers, while Ru WOCs with polypyridine and water ligands are brightly colored – having strong MLCT transitions – only in the initial Ru^{II} oxidation state. When used in photo-anodes under the applied potential, these Ru-WOCs quickly oxidize to the Ru^{III} state, lacking strong MLCT and unable to function as photosensitizers. We are also unaware of Ru-based photosensitizers with sufficient oxidative potential to deliver above ≈+1.6 V vs NHE required to drive Ru-WOCs at pH = 1.

Using Mott-Schottky analysis, the flat-band position of the materials (valence band (VB) and conduction band (CB)) is calculated. In a three-electrode setup, Mott-Schottky plots with and without light were acquired using impendence spectroscopy for **MOFs 1**, **2**, and **3**. All MOF electrodes have a positive slope of the C^{-2} F(E) function, confirming their n-type semiconducting properties. Mott-Schottky plots show the flat band potential which is the VB potential for n-type semiconducting material. These plots of **MOFs 1**, **2**, and **3** depict the position of the VB at −0.27 V and −0.31 V versus NHE for **MOF 1** with and without light, and also −0.28 V and −0.16 V versus NHE with and without light (Figure S25, Supporting Information). The position of the flat band shifted to anodic potential in **MOFs 2** and **3**, which indicates that the number of charge carriers increased after the immobilization of the Ru catalyst in the MOFs, similar to reports for the α-Fe_2O_3 photoanodes.[71–73] Due to the increase in charge-carrier density, the flat band position shifted to anodic potential after illumination and the photoelectrochemical properties of photoanodes are enhanced.[74] From the Kubelka-Munk plots and Mott-Schottky plots, we found the position of the CB and VB of **MOFs 1**, **2**, and **3**, as shown in Figure 4c. Such energy bands imply that from a thermodynamic standpoint, **MOFs 2** and **3** are viable photocatalysts for the water-splitting reaction (Figure 4c).

2.4. O_2 Evolution Using MOFs

The O_2 evolution activity of the prepared MOFs was also characterized by using CAN at pH = 1 in a Clark-type oxygen electrode of an Oxygraph. The MOFs were mixed with 0.1 M HNO_3 for 30 minutes for ligand exchange from the Ru–Cl moiety to Ru-(H_2O). The rate of O_2 evolution was measured as a function

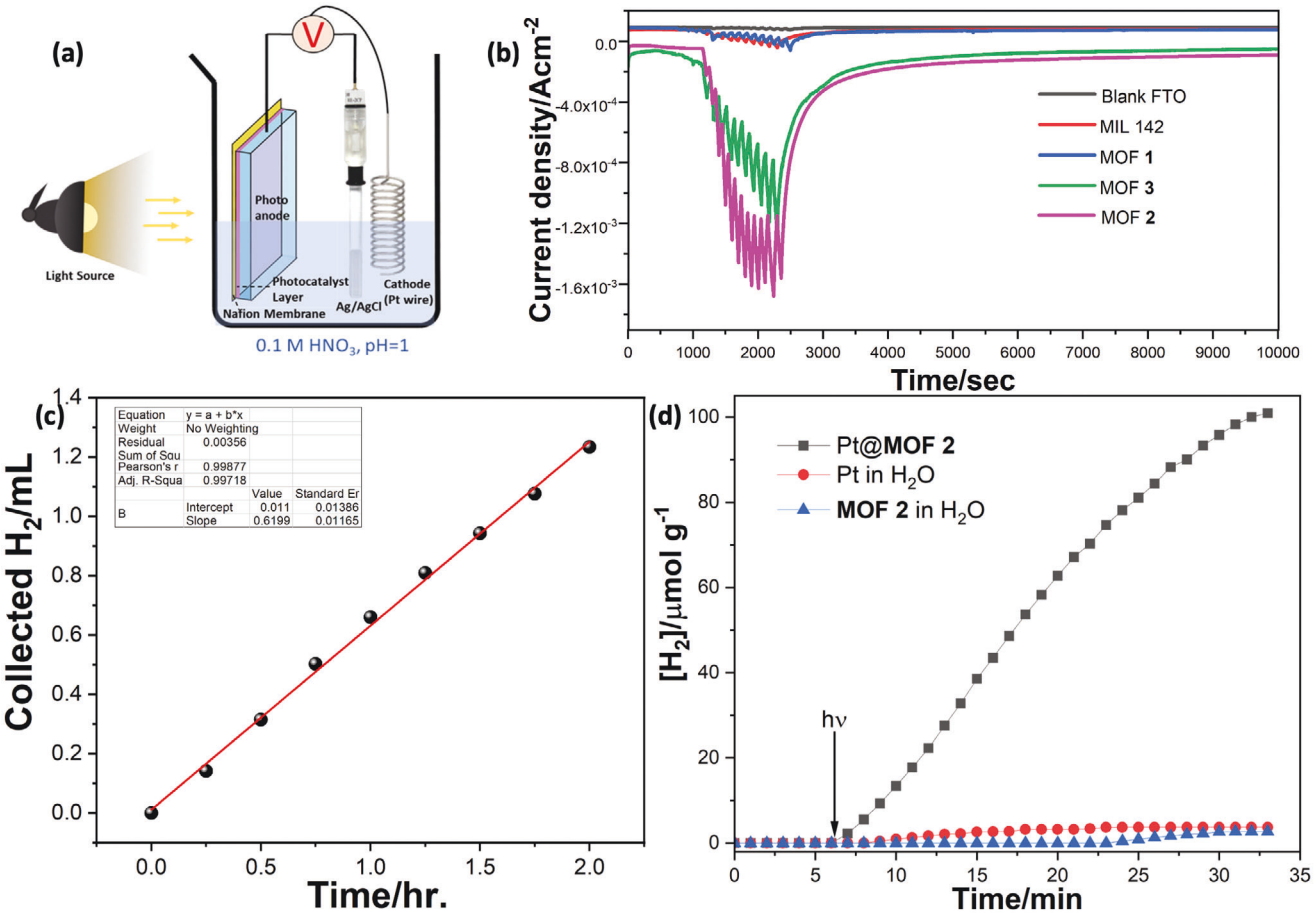

Figure 5. a) Photo-electrochemical cell containing FTO electrode drop casted with the **MOF**-based photoanode confined with Nafion membrane, Pt wire as cathode, and a Ag/AgCl reference electrode in 0.1 M HNO_3 electrolyte (pH = 1). b) Photoelectrocatalytic performance of the **MOF 2** and **MOF 3** photoanodes at pH = 1. 10 light/dark cycles (1 minute light/1 minute dark) were applied 10 minutes after the +1.4 V vs AgCl/Cl potential was applied to the activated electrode assembly. Compared are clean FTO, **MIL-142 Fe MOF**, and **MOF 1-3**. c) Rate of hydrogen collected during photo-electrochemical water oxidation with the **MOF 2** photoanode confined with Nafion membrane, Pt wire as cathode, and an +1.4 V vs Ag/AgCl reference electrode in 0.1 M HNO_3. d) Photocatalytic H_2 evolution using **MOF 2** and Pt as co-catalyst.

of time. These results show that **MOF 2** oxidizes water with excess CAN with an initial oxygen evolution rate of ≈18.33 mM s^{-1} (Figure 3c; Figure S26, Supporting Information). Undoped Fe-MOFs (Fe MIL-142 and **MOF 1**) were also examined in the presence of CAN oxidation at pH = 1; no oxygen evolution was observed in the case of MIL-142 Fe MOF, but **MOF 1** shows minor O_2 evolution: ≈2.62 mM s^{-1}. Hence, the Ru complex integrated into MOF acts as a catalyst for O_2 evolution. ICP-MS measurements before and after chemical (CAN) water oxidation at pH = 1 for **MOF 2** showed the Fe/Ru change from from 9.14 (initial) to 7.3 (after catalysis), demonstrating the retention of a substantial quantity of the Ru complex within the pores and agrees with observed structural integrity of the MOF shown in PXRD and SEM (Figures S19 and S20c,e, Supporting Information).

2.5. Photo-Electrocatalysis Using MOFs

In earlier studies, it was found that the Fe-based MOFs were active in photochemical catalysis, in the presence of a Ru-based photosensitizer ($[Ru(bpy)_3]^{2+}$) and an electron acceptor ($Na_2S_2O_8$).[45,75] In our system, we combined the light-activated Fe_3O nodes with the BDC, BTB, and H_3-Tpy linkers, allowing the MOF to coordinate WOC containing widely used tpy ligand. The photoanode layer on the FTO electrode was prepared by drop-casting the ink made from powder MOF with Nafion solution as a binder. Controlled potential electrolysis was performed at pH≈1 by using a 3-electrode system in an electrochemical cell (MOF-based photoanode with a Nafion membrane, Pt wire as a cathode, and an Ag/AgCl reference electrode at +1.4 V vs Ag/AgCl). First, the i-t curves of electrodes were recorded without light ("dark," **Figure** 5a).

All MOFs investigated in this study demonstrate current response when irradiated with visible light. Among the tested MOFs, **MIL-142** and **MOF 1** demonstrated the lowest level of activity in agreement with a lack of WOC, while **MOF 2**, and **MOF 3** exhibited the highest photocurrents (Figure 5b). Notably, **MOF 2** and **MOF 3** displayed ≈1.6×10^{-3} A·cm^{-2} and 1.2×10^{-3} A·cm^{-2}, photocurrents, respectively, at +1.4 V vs Ag/AgCl applied potential in 0.1 M HNO_3 (Figure 5b; Figure S27, Supporting

Table 1. Comparison of the of current density shown by different mononuclear Ru complexes doped MOFs.

Type of system	Potential (V vs Ag/AgCl)	Current density [A cm^{-2}]	pH	Refs.
UIO-67@[Ru(tpy)(dcbpy)(H_2O)]$^{2+}$	1.5	6.5×10^{-5} [a]	7	[33]
UIO-67@[Ru(tpy)(dcbpy)(H_2O)]$^{2+}$	1.5	1.1×10^{-5} [a]	8	[39]
UIO-67@[Ru(bpy)(dcbpy)(H_2O)$_2$]$^{2+}$	1.4	2.5×10^{-5} [a]	1	[41]
MIL-126@[Ru(bpy)(dcbpy)(H_2O)$_2$]$^{2+}$	1.4	6.5×10^{-4} [b]	1	[52]
NU-1000@[Ru(tda)(py(PhCOOH)$_2$)$_2$]	1.3	1.8×10^{-4} [a]	7	[40]
MIL-142@[Ru(H_3-Tpy)(Qc)(H_2O)]$^{+}$	1.4	1.6×10^{-3} [b]	1	This work
MIL-142@[Ru(H_3-Tpy)(Qc)(H_2O)]$^{+}$	1.4	3.8×10^{-4} [b]	7	This work

[a] The current density obtained during electrochemical water oxidation and [b] the current density obtained during photo-electrocatalytic water oxidation.

Information). The high current density obtained for **MOF 2** and **MOF 3** suggests that this Ru-doped MIL-142 is more active towards photo-electrocatalytic water oxidation than the previously reported system of [Ru(bpy)(dcbpy)(H_2O)$_2$]$^{2+}$/MIL-126 Fe-based MOFs by ≈3 times (Table S4, Figure S27, Supporting Information).[52] Values of demonstrated photocurrent (1.6×10^{-3} A·cm^{-2}) compare favorably with the best reported in the field (≈15×10^{-3} A·cm^{-2}) achieved with significantly more complex engineering of the dual junction solar cell and high loadings of RuO_2 catalyst.[76] Overall, since the early reports on the engineering of WOC into MOFs, we have achieved two orders of magnitude increase in anodic WOC current, **Table 1**. The quantum yield of ≈3.1% was determined based on our lamp characteristics and the geometry of the setup. The conductivity measurements of MOFs **1**, **2**, and **3** (Table S5, Supporting Information) show that these MOFs are poor conductors. Therefore, we hypothesize that the electron transfers – likely occurring via electron hopping – limit the performance. Moreover, controlled potential electrolysis was performed under a neutral pH≈7 using a **MOF-2** photoanode in the same three-electrode system. The resulting current density was ≈3.8×10^{-4} A·cm^{-2} (Figure S28, Supporting Information). We attribute this limited performance to a decreased function of Nafion as a proton conductor in neutral pH. To exclude the possibility of the molecular catalyst leaching in the solution, UV-vis spectra of the electrolyte were collected before and after the electrocatalysis (Figure S29, Supporting Information). No change in the UV–vis spectra suggests no leeching of molecular catalyst into the electrolyte. The ICP-MS of the electrolyte after electrocatalysis also showed no signs of Ru in the solution. PXRD (Figure S19, Supporting Information) of **MOF 2** and **MOF 3** after 24hr of catalysis at pH = 1 and SEM results after catalysis (Figure S20d,f, Supporting Information) demonstrated the structural integrity of materials.

The high activity of **MOF 2** allowed us to collect hydrogen gas at the Pt cathode coupled with a scaled-up photoanode under continuous illumination and at the +1.4 V versus Ag/AgCl applied potential, the same as used in Figure 5c. The identification of gas as hydrogen was confirmed by using a semiconductor-based hydrogen detection system (Figure S30, Supporting Information). Furthermore, H_2 gas was collected within a closed system (Figure S31, Supporting Information), demonstrating a hydrogen evolution rate of ≈ 0.62 mL hr^{-1}. Over two hours, a total of 1.2 mL of H_2 was collected from ≈6.25 cm^2 area of photoelectrode (Figure 5c). The simplicity of the system's design further enhances its practicality for large-scale production; by employing only MOF deposition on FTO glass and Nafion, the system can be easily manufactured. Considering the high activity exhibited by the Ru-doped MIL-142 MOF (**MOF 2**) system, coupled with its straightforward manufacturing process and potential for scaling, it emerges as a promising candidate for solar hydrogen production in a convenient and easily replicable prototype.

2.6. Unassisted Photocatalytic H_2 Evolution

The high activity of **MOF 2** and **MOF 3** photoanodes with a turn-on voltage (≈0.9 V at pH = 1, Figure S32, Supporting Information) below the thermodynamic potential for water splitting and the negative position of the valence band in these materials prompted us to test for unassisted light-driven water splitting. Previous investigations have established that platinum can function as a co-catalyst or a site for hydrogen evolution in photochemical reactions involving water splitting when combined with a primary photocatalyst, such as titanium dioxide (TiO_2).[77,78] Hence Pt co-catalyst was introduced into the pores of **MOF 2** through an in situ photoreduction process using H_2PtCl_4.[79] Upon exposure of Pt@**MOF 2** to visible light, the evolution of H_2 over time was monitored using a semiconductor-based hydrogen detection system within a closed system. The maximum amount of evolved H_2 observed was 101 µmol g^{-1}, with a rate of 4.8 µmol g^{-1} min^{-1} (Figure 5d; Figure S33, Supporting Information). To the best of our knowledge, this is the most active MOF assembly revolving H_2 under illumination without the use of a sacrificial electron donor.

Additionally, since the early reports on the engineering of WOC into MOFs, we have achieved two orders of magnitude increase in anodic WOC current, **Table 1**. With the next single order of magnitude increase, these simple-to-process systems will beat the best-in-field: highly complex and non-scalable, multiple-junction solar cells, utilizing high content of Ir or Ru oxides. Further improvements are possible with increased electrical conductivity of MOFs, increased lifetime of light-induced charge-separated states in the MOF, and with the integration of faster and lower overpotential WOC catalysts designed with 3d transition metals.

3. Conclusion

We successfully utilized the WOCs having *trans*-[Ru(R-tpy)(Qc)(H_2O)]$^{+}$ scaffold, wherein the addition of negatively charged QC ligands not only improved catalytic activity but also eradicated the lag phase in chemically driven water oxidation, affirming the true catalyst nature of the starting Ru complex. Specifically, **WOC 1** emerged as the most effective catalyst operating via the WNA mechanism and thus suitable for device integration. For light-induced water oxidation catalysis, we integrated *trans*-[Ru(tpy)(Qc)(H_2O)]$^{+}$ into the MIL-142 Fe MOF. Employing innovative ligand design, we successfully incorporated the Ru WOC into the MOF structure, yielding **MOFs 2** and **3**. These catalyst-incorporated MOFs have enhanced

performance in both chemical and photo-electrochemical water oxidation processes while Pt@**MOF 2** supports the unassisted light-driven water splitting. The simplicity of the photoanode design further enhances its practicality for large-scale use; by employing only MOF deposition onto FTO glass and Nafion, the system can be easily manufactured. Considering the high activity coupled with its straightforward manufacturing process and potential for scaling, it emerges as a promising candidate for solar hydrogen production in a convenient and easily scalable prototype. The continuous advancement in anodic WOC current underscores the possibility that these simple-to-process MOF-based systems will emerge as a challenger to earlier reported highly complex and non-scalable, multiple-junction solar cells, utilizing high content of Ir or Ru oxides light-driven water splitting devices. Further improvements are possible with increased electrical conductivity of MOFs, increased lifetime of light-induced charge-separated states in the MOF, and with the integration of faster WOC catalysts with lower overpotential designed with 3d transition metals. In this trajectory, the convergence of innovation and simplicity paves the way for promising strides in scalable solar hydrogen production for sustainable energy.

4. Experimental Section

General Information: All chemicals and solvents were purchased from Sigma Aldrich, Fisher Scientific, and TCI America and were used as received. NMR spectra were recorded on a Bruker AV-III-HD-400 400 MHz spectrometer, and chemical shifts were referenced to solvent residual peaks. UV-vis spectra were recorded on a Varian Cary 300- Bio spectrophotometer. Aqueous solutions were prepared using ultrapure (Type 1) water (resistivity 18.2 MΩ·cm at 25 °C) from a Q-POD unit of Milli-Q integral water purification system (Millipore, Billerica, MA, USA). Solvents and chemicals were purchased from Sigma-Aldrich (St. Louis, MO, USA) and were used without further purification. PXRD data were collected using Panalytical Empyrean Powder X-ray diffractometer. All SEM imaging was undertaken on a Zeiss EVO LS15 SEM using 5 kV accelerating voltage, a probe current of 15–40 pA, and a working distance of 8–15 mm. Diffuse reflectance spectra were recorded using a Lambda 950 UV-Vis spectrophotometer. The XPS data were collected using Kratos AXIS Ultra DLD Imaging X-ray Photoelectron Spectrometer at the Surface Analysis Facility of the Birck Nanotechnology Center at Purdue University. The binding energies of the elements were calibrated with the adventitious C 1s located at 283.5 eV (C-C).

EPR: X-band EPR measurements were performed on an EMX X-band spectrometer equipped with an X-Band CW microwave bridge (Bruker, Billerica, MA, USA). Samples were oxidized with ammonium cerium nitrate (CAN) and frozen in liquid nitrogen within 30s. During EPR measurements, the sample temperature was maintained at 20 K using a closed-cycle cryostat (ColdEdge Technologies, Allentown, PA, USA). Spectrometer conditions were as follows: microwave frequency 9.47 GHz; field modulation amplitude 25 G at 100 kHz, microwave power 31.7 mW, unless otherwise mentioned. Measurements were performed on the same day in the same conditions, to allow accurate comparison of signal intensities.

Electrochemistry: Cyclic voltammetry was accomplished using a potentiostat (CHI 627C; CH Instruments Inc., Austin, TX, USA) using a standard single-compartment 3-electrode cell. Boron-doped diamond electrode (BDD) with a diameter 3 mm, served as working, a piece of a platinum wire in an auxiliary chamber served as the counter electrode, and a saturated Ag/AgCl electrode served as the reference electrode. Electrolytes were saturated with argon prior to the measurements. The half-wave potentials ($E_{1/2}$) of the reported complexes in this work were determined as the average of the anodic and cathodic peak potentials ($E_{1/2} = (E_{pa} + E_{pc})/2$) from the cyclic voltammetry. From the peak-to-peak separations ΔE_p ($\Delta E_p = E_{pa} - E_{pc}$), as well as the ratio of the anodic to cathodic peak currents (i_{pa}/i_{pc}), the reversibility of the redox couples were determined. All reported measurements were repeated several times to ensure the reproducibility of results.

Photoanode Fabrication: Photoanodes were prepared by using drop casting of catalytically active MOFs was performed according to the reported procedure.[52] For each electrode, the ink was prepared by suspending 8 mg of MOF in 0.8 mL of isopropanol with the addition of 20 µL of Nafion solution (5% in alcohol/water, Sigma Aldrich Inc.). After, the suspended mixture was layered and drop casted on an FTO electrode surface, and complete evaporation of isopropanol was observed prior to depositing successive layers. Five layers of the suspended MOF mixture were deposited. After drop casting, the MOF-bearing electrodes were dried by air at room temperature.

Mott-Schottky Studies: Mott-Schottky studies with a Biologic SAS VMP3 electrochemical workstation in a standard three-electrode electrochemical cell. The fabricated photoanode of **MOF 1**, **MOF 2,** and **MOF 3** were taken as working electrodes. The Ag/AgCl and platinum coil were used as reference and counter electrodes in 0.1 M HNO_3 aqueous electrolyte. The potentiation impedance spectroscopy (PEIS) was recorded from −0.1 to 1.6 V vs Ag/AgCl, using sinusoidal wave having 10 mV amplitude at frequencies 1, 2, 2.5 3, 3.5, 4, 4.5, 8, 9, and 9.5 kHz in the dark condition and in the presence of light (600 W, visible light). A graph was drawn between 1/C2 vs Potential (V) vs NHE. By extrapolating the linear region of the graph, the X-intercept was determined, which gives the value of the flat-band position. All the MOF photoanodes possess a positive slope indicating the n-type behavior with flat-band which represented the CB position.[80]

Photo-Electro Catalysis: Photoelectrochemical catalysis was performed by using a single-compartment 3-electrode cell. A drop-casted MOF photoanode (surface area 1 cm^2) was firmly covered by a proton-exchange Nafion membrane, and the bottom of the assembly was dipped into 0.1 M nitric acid solution (pH = 1). A platinum wire was used as the counter electrode auxiliary chamber, and a saturated Ag/AgCl electrode was used as the reference electrode. Anodes were illuminated with an unfocused 500 W light source, and UV light was filtered out. All reported measurements were repeated several times to ensure the reproducibility of results.

Detection of H_2 Using a Semiconductor-Based Hydrogen Detection System: The detection of hydrogen gas in this study was carried out using a semiconductor-based hydrogen detector known as MQ-8 Hydrogen Sensor.[81] In the absence of hydrogen gas, the detector exhibits a resistance denoted as Ro. However, upon contact with hydrogen gas, the conductivity of the detector increases, resulting in a reduction in resistance, denoted as Rs. Thus, the concentration of hydrogen gas can be estimated by calculating the ratio of Rs to Ro, denoted as Rs/Ro. To calibrate the MQ-8 semiconductor-based hydrogen detector, a sample of 99.99% pure hydrogen was utilized in this experiment. At a H_2 concentration of 0 ppm, the value of Rs/Ro was measured to be 1. As the hydrogen concentration increases, the value of Rs/Ro decreases logarithmically, ranging from 0.09 at 1000 ppm to 0.04 at 10,000 ppm. The measurement of hydrogen gas generation was recorded in ppm by connecting the change in Rs/Ro to a microcontroller, which facilitated the transmission of data to a computer memory via the Arduino Uno Software.[82] The setup and arrangement of the experimental apparatus were visually illustrated in Figure S32 (Supporting Information).

Photocatalytic H_2 Evolution: The photocatalytic H_2 production was also carried out by using **MOF 2** as primary catalyst and Pt as the co-catalyst in water without any sacrificial electron donor. The **MOF 2** of 5 mg was dispersed in 2 mL of water, H_2PtCl_6 was added to the final concentration of 0.1 mM, and the mixture was degassed by bubbling N_2 for 10 min before irradiation with 320 nm UV flashlight lamp to deposit Pt.[79] Under an unfocused 500 W light source (UV light was filtered out) H_2 evolution was recorded as a function of time with the help of the semiconductor-based hydrogen detection system in a closed system.

ICP-MS Measurement: ICP-MS analysis was conducted on a Thermo Scientific Element 2 mass spectrometer equipped with a Teledyne Cetac

Aridus II nebulizer. The Ru-doped MOF samples were digested in 70% ultrahigh purity nitric acid (Seastar Chemicals) at 90 °C for 12 h. The solution was then diluted 35 times with water and purified by filtration through a 0.2 µm syringe filter. Further dilutions were performed with 2% ultrapure nitric acid, 5 ppb In were added to the calibration standard, and samples as the internal control. ^{56}Fe and ^{99}Ru under medium resolution were monitored for Fe and Ru quantification.

Conductivity Measurement: MOF conductivity was measured using a prototype device consisting of a sheet of brass, and an FTO glass (Figure S23, Supporting Information, 5 mg) separated[52] with nonconductive tape with a thickness of 0.1 mm. Ohm's law was used to determine the resistance, and since the thickness and surface area of the resistor were known, the MOF conductivity was calculated. As was noted previously, the exact results of conductivity measurements might differ based on the used technique, but such differences were typically less than one order of magnitude.[83] Thus, one should consider the method of measurement before any direct comparison of the MOF conductivity for different MOFs. Xie et al. reported four different measurement methods and noted that errors were typically larger for materials with low conductivity due to the sensitivity limitations of measurement devices.[83]

FTIR Spectroscopy: A Thermo Nicolet Nexus FTIR Spectrometer was used for FTIR measurements. The device was run on OMNIC software. Some of the specifications of the device were an MCT detector and a KBr beam splitter. The interior space of the spectrometer was continuously purged with nitrogen gas for at least one hour before the measurement to reduce the background from water vapor. Data collection used a small amount of the dry powder sample pressed against an attenuated total reflectance (ATR) diamond crystal by a handle, and the measurements were done at room temperature. The graph consists of 36 scans with 4 cm^{-1} resolution.

O_2 Evolution: Oxygen evolution was measured with a Clark-type polarographic oxygen electrode with an Oxygraph System (Hansatech Instruments Ltd., King's Lynn, Norfolk, UK). Calibration was performed by measuring signal in O_2-saturated deionized water and then adding sodium dithionite (an oxygen-depleting agent). The drop in the signal was set equal to the solubility of oxygen in water at room temperature (262 µmol L^{-1}).

In chemical catalysis, the borosilicate vessel was filled with 500 µL solutions of the complex at pH = 1 (in 0.1 M nitric acid) and was constantly stirred. 20 mM. of CAN dissolved in nitric acid at pH = 1 was added to the chamber and oxygen concentration was recorded as a function of time.

For the chemical O_2 evolution for the MOF, 5 mg of FeMIL142-H_3Tpy-Ru(Qc) MOF was added to 0.3 ml of 0.1 M HNO_3, soaked for 30 minutes, added to Oxygraph System chamber and constantly stirred followed by addition of 0.3 ml of 400 mM CAN. Oxygen concentration was recorded as a function of time.

DFT Calculation: Density functional theory calculations were performed at the UB3LYP level of theory, with the DGDZVP basis set for the ruthenium atoms, and the 6–31G* basis set was used for light (C, H, N, O) atoms. All molecules were modelled in water using the Conductor Polarized Continuum Model (CPCM) solvation model. All redox potentials were calculated using the DFT-calculated free energies of the products minus the reactants. From this value, 4.44 V was subtracted to account for the NHE voltage. The free energy of solvation for H^+ was taken to be −11.64 eV. Geometries of intermediates were optimized, then electronic/thermal energies and vibrational frequencies were calculated as single-point calculations upon the optimized states.

Synthesis: The R-tpy ligands, the precursor complex Ru(R-tpy)Cl_3 and Ru(Qc)(p-cymene)Cl were prepared following the literature procedure.[7,8,41,57]

Synthesis of [Ru(R-tpy)(Qc)Cl]: [$RuCl_3$(R-tpy)] of 100 mg, 55 mg of 8-quinoline carboxylate (Qc), and NEt_3 (0.2 mL) were dissolved in 20 mL of degassed ethanol in a 100 mL round bottom flask. The reaction mixture was refluxed at 100° C for 6 h under nitrogen atmosphere. The mixture was then evaporated until dry, and the resulting dark solid was dissolved in 5 mL of CH_2Cl_2 and purified by chromatography using a neutral alumina column. The blue-violet solution corresponding to the major isomer *trans-* was eluted first with CH_2Cl_2:CH_3OH (20:1), followed by the red-violet solution of the minor isomer *cis-* with CH_2Cl_2:CH_3OH (10:1) mixture. Upon removal of the solvent under reduced pressure, the pure isomeric complexes trans-1 and cis-1 were obtained in the solid state. The collected compounds were characterized as [Ru(R-tpy)(Qc)Cl] by ^{1}H NMR and ^{13}C NMR.

trans-[Ru(tpy)(Qc)Cl]: Yield: 85 mg, 69.6% based on Ru. HRMS (ESI): Calc. for $C_{25}H_{17}N_4ClO_2Ru$ [Ru(tpy)(Qc)Cl]$^+$ m/z 542.01 found 542.03. ^{1}H NMR (DMSO-d6): δ 10.40 (s, 1H) 8.77 (d, 1H, J = 12 Hz), 8.61 (m, 4H), 8.48 (d, 1H, J = 12 Hz), 8.37 (d, 1H, J = 8 Hz), 7.89 (m, 6H), 7.75 (t, 1H, J = 16 Hz), 7.38 (t, 2H, J = 16 Hz).

Cis-[Ru(tpy)(Qc)Cl]: Yield: 5 mg, 4% based on Ru. ^{1}H NMR (DMSO-d6): δ 8.98(d, 1H, J = 7.2 Hz) 8.57 (m, 6H), 8.03 (d, 1H, J = 6.8 Hz), 7.91 (t, 3H, J = 6.8 Hz), 7.79 (t, 1H, J = 6.8 Hz), 7.7 (t, 1H, J = 8.4 Hz), 7.54 (t, 3H, J = 6.6 Hz), 7.03 (d, 1H, J = 10.2 Hz), 6.79 (dd, 1H, J = 5.6 Hz, J = 8 Hz).

trans-[Ru(Cl-tpy)(Qc)Cl]: Yield: 81 mg, 67% based on Ru. HRMS (ESI): Calc. for $C_{25}H_{16}N_4Cl_2O_2Ru$ [Ru(Cl-tpy)(Qc)Cl]$^+$ m/z 575.97 found 576.01. ^{1}H NMR (DMSO-d6): δ 10.38 (d, 1H, J = 4 Hz), 8.86 (s, 1H), 8.80 (d, 2H, J = 8 Hz), 8.70 (d, 2H, J = 8 Hz), 8.48 (d, 1H, J = 12 Hz), 8.38 (d, 1H, J = 8 Hz), 7.96 (m, 5H), 7.75 (t, 1H, J = 4 Hz), 7.42 (t, 2H, J = 4 Hz).

Cis-[Ru(Cl-tpy)(Qc)Cl]: Yield: 5 mg, 4% based on Ru. ^{1}H NMR (DMSO-d6): δ 9.353 (s, 3H) 8.89 (d, 3H, J = 8 Hz), 8.47 (m, 1H), 8.02 (m, 4H), 7.56 (d, 3H, J = 2 Hz), 7.25 (t, 3H, J = 8 Hz)

trans-[Ru(EtO-tpy)(Qc)Cl]: Yield: 87 mg, 72% based on Ru. HRMS (ESI): Calc. for $C_{27}H_{21}N_4ClO_3Ru$ [Ru(Cl-EtO-tpy)(Qc)Cl]$^+$ m/z 586.03 found 586.01. ^{1}H NMR (DMSO-d6): δ 10.36 (s, 1H), 8.75 (d, 1H, J = 12 Hz), 8.63 (d, 2H, J = 4 Hz), 8.51 (d, 1H, J = 4 Hz), 8.36 (dd, 4H, J = 8 Hz), 7.89 (m, 3H), 7.84 (t, 1H, J = 4 Hz), 7.36 (t, 3H, J = 8.2 Hz), 4.50 (t, 2H, J = 12 Hz), 1.51 (t, 3H, J = 4 Hz).

Cis-[Ru(EtO-tpy)(Qc)Cl]: Yield: 3.8 mg, 3% based on Ru. ^{1}H NMR (DMSO-d6): δ 8.93 (s, 2H) 8.73 (d, 2H, J = 8 Hz), 8.62 (d, 2H, J = 6.8 Hz), 8.34 (s, 4H), 7.81 (m, 3H), 7.52 (t, 1H, J = 6.4 Hz), 4.44 (t, 2H, J = 7.6 Hz), 1.504 (s, 3H).

Synthesis of [Ru(R-tpy)(Qc)(H_2O)](PF_6): 100 mg of *trans-*[Ru(R-tpy)(Qc)Cl] was dissolved in 20 mL of an acetone/water (3:1, v/v) mixture in a 50 mL round-bottom flask, and 60 mg of $AgNO_3$ was added to the solution and stirred for 3 h at reflux. The initial blue-violet color of the solution changed to red-violet with the precipitation of AgCl. To remove the AgCl undissolved solid, the cooled solution was filtered over Celite. The filtrate was then concentrated to approximately 2 mL under vacuum, and 3 mL of a saturated solution of NH_4PF_6 was added. The resulting solution was allowed to stand at 0 °C for complete precipitation. It was then filtered, and the product was washed with ice-cold water several times and dried under a vacuum. The collected compounds were characterized as [Ru(R-tpy)(Qc)(H_2O)](PF_6) by ^{1}H NMR and ^{13}C NMR.

trans-[Ru(tpy)(Qc)(H_2O)](PF_6) (WOC 1): Yield: 107 mg, 87% based on Ru. ^{1}H NMR (DMSO-d6): δ 10.19 (d, 1H, J = 12 Hz) 8.86 (d, 1H, J = 1.6 Hz), 8.77 (d, 2H, J = 8.4 Hz), 8.71 (d, 2H, J = 6 Hz), 8.34 (m, 3H), 8.17 (t, 2H, J = 4.8 Hz), 7.98 (m, 3H), 7.48 (t, 1H, J = 7.48 Hz) 7.52 (t, 1H, J = 1.6 Hz).

trans-[Ru(Cl-tpy)(Qc)(H_2O)](PF_6) (WOC 2): Yield: 103 mg, 84% based on Ru. ^{1}H NMR (DMSO-d6): δ 10.38 (d, 1H, J = 3.6 Hz), 8.86 (m, 2H), 8.81 (d, 1H, J = 1.6 Hz), 8.68 (d, 2H, J = 1.2 Hz), 8.48 (d, 1H, J = 7.2 Hz), 8.38 (d, 1H, J = 10 Hz), 7.98 (d, 2H, J = 5.2 Hz), 7.93 (m, 3H), 7.75 (t, 1H, J = 1.6 Hz) 7.42 (t, 2H, J = 7.2 Hz).

trans-[Ru(EtO-tpy)(Qc)(H_2O)](PF_6) (WOC 3): Yield: 98 mg, 80% based on Ru. ^{1}H NMR (DMSO-d6): δ 10.18 (d, 1H, J = 16 Hz), 8.79 (dd, 3H, J = 1.6 Hz, J = 8 Hz), 8.44 (s, 2H), 8.37 (dd, 2H, J = 6.4 Hz, J = 5.6 Hz), 8.16 (t, 2H, J = 4 Hz), 7.97 (d, 2H, J = 5.6 Hz), 7.92 (d, 1H, J = 5.2 Hz), 7.76 (t, 1H, J = 11 Hz), 7.48 (t, 2H, J = 3.8 Hz), 4.48 (t, 2H, J = 7 Hz), 1.49 (t, 3H, J = 7 Hz).

Synthesis of 1-(5-methylpyridin-2-yl)ethan-1-one (L_1): In a 100 mL RB flask, 1 g of 2-bromo-5-methylpyridine was dissolved in 12 mL dry Et_2O. The mixture was cooled to −78 °C with liquid N_2 and EtOH. To the cooled solution n-BuLi (3 mL) was added dropwise. The reaction mixture was stirred at −78 °C for 90 mins, 10 mL dimethylacetamide (DMA) was added and allowed to react for another 5 h at room temperature. The reaction mixture was then quenched with NH_4Cl saturated aqueous solution. The

Et_2O layer was separated, and the aqueous layer was extracted with Et_2O several times. The organic parts were dried with anhydrous Na_2SO_4 and the organic solvent was removed under vacuum. The obtained liquid was further purified by column chromatography ($EtOAc/CH_2Cl_2$) to get a colorless oil product. ^1H NMR ($CDCl_3$-d): δ 8.42 (s, 1H), 7.85 (d, 1H, J = 8 Hz), 7.55 (d, 1H, J = 12 Hz), 2.61 (d, 3H), 2.35 (s, 3H).

Synthesis of 4-(5,5′′-dimethyl-[2,2′:6′,2′′-terpyridin]−4′-yl)benzoic acid: In a 250 mL round bottom flask, 1gm of synthesized 5-methyl acetyle pyridine and 0.566 gm of 4-carboxybenzaldehyde dissolved in 18 mL MeOH, and 15% KOH aqueous solution (25 mL) and $NH_3{\cdot}H_2O$ (10 mL) were allowed to react for three days at room temperature. White precipitate came out, which was filtered and washed with $CHCl_3$ several times. The obtained solid was then dissolved in a mixture of $MeOH/H_2O$ (v/v = 1/1), followed by the addition of 1 M HCl until pH = 3. The obtained solid was formed, filtered, washed with water, and dried to give solid white product. ^1H NMR ($CDCl_3$-d): δ 8.74 (s, 1H), 8.86 (t, 2H, J = 4 Hz), 8.15 (d, 1H, J = 6.4 Hz), 8.09 (d, 1H, J = 6.8 Hz), 7.95 (d, 1H, J = 5.6 Hz), 2.44 (s, 3H).

Synthesis of 4′-(4-carboxyphenyl)-[2,2′:6′,2′′-terpyridine]−5,5′′-dicarboxylic acid (H_3-Tpy): 0.2 g of the synthesized L_2 was dissolved with, pyridine/H_2O (v/v = 4/1, 20 mL) in a 250 mL three-necked flask. The reaction mixture was heated, and 1.8 gm KMnO4 was added in successive portions with 0.4 g each time. The system was refluxed overnight, and after, was cooled, filtered, and the dark filter cake was washed with methanol several times. The obtained clear filtrates were combined, and the organic solvent was removed under vacuum. The residual aqueous part was acidified with 6 M hydrochloric acid to adjust pH to 3. White precipitate was formed, filtered, washed with water serval times, and air-dried. ^1H NMR (DMSO-d6): δ 13.417 (s, 1H), 9.25 (s, 1H), 8.86 (s, 1H), 8.82 (d, 1H, J = 6.4 Hz), 8.51 (dd, 1H, J = 4 Hz), 8.16 (d, 1H, J = 6.4 Hz), 8.10 (d, 1H, J = 4 Hz).

Synthesis of Ru(Qc)(p-cymene)Cl: 200 mg of $[Ru(p\text{-cymene})Cl_2]_2$ (0.205 mmol) and 113 mg of 8-quinoline carboxylate (2 equiv) were dissolved in 20 ml of ethanol. To the ethanolic mixture, NEt_3 (0.2 mL) was added and refluxed for 3 hours in a round bottom flask with a reflux condenser under argon. After cooling, a solvent was removed under vacuum. The resulting residue was dissolved in ≈5 ml of ethanol followed by trituration with 30 ml of diethyl ether to obtain an orange-colored precipitate. The precipitate was filtered and dried on air. The collected compound was characterized by ^1H NMR. The yield was 180 mg, (80%). ^1H NMR (400 MHz, $CDCl_3$-d) δ 8.88 (dd, 2H, J = 2 Hz, J = 7.2 Hz), 8.42 (d, 1H, J = 8), 8.11 (d, 1H, J = 4 Hz), 7.78 (t, 1H, J = 4.2 Hz), 7.63 (d, 1H, J = 12.8 Hz), 2.9 (t, 1H, J = 7.2 Hz), 2.15 (s, 3H), 1.26 (s, 6H).

Synthesis of [Ru(Qc)(H_3-Tpy)Cl]: 100 mg of Ru(p-cymene)(Qc)Cl (0.225 mmol) and 99 mg of H_3-Tpy (0.237 mmol, 1.05 equiv.) were dissolved in 10 ml of N, N-dimethylformamide (DMF) in a round bottom flask and reflux for 3 hours under Ar. After cooling to room temperature, the solvent was removed under vacuum. The round bottom flask was filled with argon, and the residue was triturated with 10 ml of ethanol quickly filtered in argon flow, and dried under vacuum. The resulting dark solid was dissolved in 5 mL of CH_2Cl_2 and purified by chromatography using a neutral alumina column. The green-violet solution corresponding to the major isomer trans-1 was eluted first with CH_2Cl_2:CH_3OH (20:1) followed by the red-violet solution of the minor isomer cis-1 with CH_2Cl_2:CH_3OH (15:1) mixture. On removal of the solvent under reduced pressure, the pure isomeric complexes *trans*-1 and *cis*-1 were obtained in the solid state. The collected both trans- and cis-[Ru(Qc)(H_3-Tpy)Cl] were characterized as [Ru(H_3-Tpy)(Qc)Cl] by ^1H NMR and ^{13}C NMR.

Trans-[Ru(H_3-Tpy)(Qc)Cl]: Yield: 78 mg, 66% based on Ru. ^1H NMR (DMSO-d6): δ 9.724 (s, 1H), 8.68 (d, 1H, J = 1.56 Hz), 8.66 (t, 3H, J = 1.36 Hz), 8.32 (d, 3H, J = 1.6 Hz), 7.6 (m, 2H), 7.48 (t, 2H, J = 3.8 Hz), 7.17 (t, 1H, J = 3.8 Hz), 7.08 (t, 3H, J = 2.56 Hz), 6.77 (t, 2H, J = 3.78 Hz).

Cis-[Ru(H_3-Tpy)(Qc)Cl]: Yield: 8.5 mg, 5% based on Ru. ^1H NMR (DMSO-d6): δ 8.38 (m, 5H), 8.06 (s, 2H), 7.99 (d, 1H, J = 7.6 Hz), 7.81 (t, 1H, J = 7.4 Hz), 7.74 (t, 1H, J = 4.6 Hz), 7.72 (m, 1H), 7.47 (m, 1H), 7.36 (t, 14H, J = 6.2 Hz), 7.21 (t, 2H, J = 1.4 Hz) 7.10 (t, 3H, J = 6.4 Hz).

Synthesis of 1 mM of trans-[Ru(Qc)(H_3-Tpy)(H_2O)]$^+$: To prepare the 1 mM solution of ***trans-***[Ru(Qc)(H_3-Tpy)(H_2O)]$^+$, 7.9 mg of trans-[Ru(H_3-Tpy)(Qc)Cl] was dissolved in 10 ml of de-ionized water and then was stirred overnight, followed by the addition of 4.2 mg of $AgNO_3$ (2.5 equiv.). After being stirred overnight, the solution was filtered through a 0.2 µm syringe filter to remove the AgCl precipitate.

Synthesis of MIL-142: 12 mg of H_3BTB and 12 mg of BDC were dissolved in 3 mL DMF. A mixture of 1 mL DMF and acetic acid (0.20 mL) containing Iron(III) nitrate nona-hydrate 20 mg was then added to the solution containing H_3BTB and BDC. The reacted solution was subsequently placed in a glass 10 mL vial and heated at 120 °C for 24 h. Upon cooling the reaction mixture to room temperature, an orange precipitate was formed. The precipitate was then isolated via vacuum filtration, subjected to acetone washing, and dried overnight under ambient conditions. air. Yield 12 mg.

Synthesis of MOF 1: 40 mg of H_3BTB, 50 mg of BDC, and 10 mg of H_3-Tpy were dissolved in 4 mL DMF. A mixture of 2 mL DMF and acetic acid (0.20 mL) containing iron(III) nitrate nonahydrate (100 mg) was then added to the solution containing H_3BTB, BDC, and H_3Tpy. The reacted solution was subsequently placed in a 10 mL glass vial and heated at 120 °C for 48 h.[82] Upon cooling the reaction mixture to room temperature, an orange-brown precipitate was formed. The precipitate was isolated via vacuum filtration, subjected to acetone washing, and dried overnight under ambient conditions. Yield 137 mg. The reaction mixture filtrate was analyzed by Uv–vis and remaining absorption at ≈280 nm indicated that ≈98.4% of the supplied ligands mixture was incorporated into MOF.

Synthesis of MOF 2: 120 mg of MIL 142- H_3-Tpy MOF and 10 mg of Ru(Qc)(p-cymene)Cl complex (1:1 equiv. of precursor: H_3-Tpy) was mixed in 3 mL DMF. The reacted solution was subsequently placed in a 20 mL glass vial and heated at 120 °C for 48 h. Upon cooling the reaction mixture to room temperature, reddish-brown precipitate was formed. The precipitate was isolated via vacuum filtration, subjected to acetone washing, and dried overnight under ambient conditions. Yield 104 mg.

Synthesis of MOF 3: 50 mg of BDC, 35 mg of BTB, and 15 mg of trans-[Ru(H_3-Tpy)(Qc)Cl] were dissolved in 10 ml of DMF followed by the addition of 100 mg of $Fe(NO_3)_3$ and 20 µL of AcOH. The mixture was subsequently placed in a 20 mL glass vial and heated at 120–130° C for 48 hours. Upon cooling the reaction mixture to room temperature, a reddish-brown precipitate was formed. The precipitate was isolated via vacuum filtration, subjected to acetone washing, and dried overnight under ambient conditions. Yield 135 mg.

Supporting Information

Supporting Information is available from the Wiley Online Library or from the author.

Acknowledgements

This research was supported by NSF, CHE-2155060 (Y.P.). Access to EPR was provided by the Amy Instrumentation Facility, Department of Chemistry, under the supervision of Dr. Michael Everly. The authors thank Prof. L. Rokhinson for providing access to the Zeiss EVO LS15 electron microscope and Dr. O. Maximova for assistance with SEM measurements. The authors thank Dr. A. Lagoutchev for assistance with the diffuse reflectance spectroscopy, Dr. N. P. Dileep for electrical conductivity measurements, Dr. R. Ezhov for the helpful discussions and Dr D. Zemlyanov for his help in XPS spectra acquisition. The authors also thank to Prof. Jianguo Mei for providing access to the electrochemical workstation and Dr. Palak Mehra for assistance with Mott-Schottky plot analysis. All acknowledged scientists were affiliated with Purdue University.

Conflict of Interest

The authors declare no conflict of interest.

Data Availability Statement

The data that support the findings of this study are available from the corresponding author upon reasonable request.

Keywords

heterogeneous catalysis, homogeneous catalysis, metal-organic framework, photo-electrochemical water splitting, Ru catalysts, unassisted H_2 evolution

Received: November 6, 2023
Revised: March 11, 2024
Published online:

[1] N. S. Lewis, D. G. Nocera, *Proc. Natl. Acad. Sci. USA* **2006**, *103*, 15729.
[2] S. Perathoner, G. Centi, S. S. S. Catal, in *Stud Surf Sci Catal*, (Eds: A. Basile, G. Centi, M. De Falco, G. Iaquaniello), Elsevier, Amsterdam **2020**, pp. 415–430.
[3] A. Nawaz, A. Kuila, A. Rani, N. S. Mishra, L. C. Sim, K. H. Leong, P. Saravanan, in *Industrial Applications of Nanomaterials* (Eds: S. Thomas, Y. Grohens, Y. B. Pottathara), Elsevier, Amsterdam **2019**, pp. 151–179.
[4] C. Acar, I. Dincer, in *Comprehensive Energy Systems*, (Ed: I. Dincer), Elsevier, Oxford **2018**, pp. 1–40.
[5] D. Gust, T. A. Moore, A. L. Moore, *Acc. Chem. Res.* **2009**, *42*, 1890.
[6] J. Patel, K. Majee, S. K. Padhi, *RSC. Adv.* **2016**, *6*, 61959.
[7] J. Patel, G. Bury, A. K. Ravari, R. Ezhov, Y. Pushkar, *ChemSusChem* **2022**, *15*, 202101657.
[8] J. Patel, K. Majee, E. Ahmad, B. Das, S. K. Padhi, *Eur. J. Inorg. Chem.* **2017**, *2017*, 160.
[9] J. Patel, K. Majee, E. Ahmad, A. Vatsa, B. Das, S. K. Padhi, *ChemistrySelect* **2017**, *2*, 123.
[10] J. Patel, K. Majee, M. Raj, A. Vatsa, S. Rai, S. K. Padhi, *ChemistrySelect* **2017**, *2*, 3053.
[11] J. Chen, P. Wagner, L. Tong, G. G. Wallace, D. L. Officer, G. F. Swiegers, *Angew. Chem., Int. Ed.* **2012**, *51*, 1907.
[12] R. Brimblecombe, G. F. Swiegers, G. C. Dismukes, L. Spiccia, *Angew. Chem., Int. Ed.* **2008**, *47*, 7335.
[13] Y. Gao, J. Liu, M. Wang, Y. Na, B. Åkermark, L. Sun, *Tetrahedron* **2007**, *63*, 1987.
[14] L. Mognon, S. Mandal, C. E. Castillo, J. Fortage, F. Molton, G. Aromí, J. Benet-Buchhlolz, M.-N. Collomb, A. Llobet, *Chem. Sci.* **2016**, *7*, 3304.
[15] K. J. Young, M. K. Takase, G. W. Brudvig, *Inorg. Chem.* **2013**, *52*, 7615.
[16] R. Ezhov, A. K. Ravari, Y. Pushkar, *Angew. Chem., Int. Ed.* **2020**, *59*, 13502.
[17] S. I. Shylin, M. V. Pavliuk, L. D'Amario, F. Mamedov, J. Sá, G. Berggren, I. O. Fritsky, *Chem. Commun.* **2019**, *55*, 3335.
[18] A. Chanda, X. Shan, M. Chakrabarti, W. C. Ellis, D. L. Popescu, F. Tiago de Oliveira, D. Wang, L. Que Jr., T. J. Collins, E. Münck, E. L. Bominaar, *Inorg. Chem.* **2008**, *47*, 3669.
[19] C. Panda, J. Debgupta, D. Díaz Díaz, K. K. Singh, S. Sen Gupta, B. B. Dhar, *J. Am. Chem. Soc.* **2014**, *136*, 12273.
[20] A. Bucci, A. Savini, L. Rocchigiani, C. Zuccaccia, S. Rizzato, A. Albinati, A. Llobet, A. Macchioni, *Organometallics* **2012**, *31*, 8071.
[21] D. B. Grotjahn, D. B. Brown, J. K. Martin, D. C. Marelius, M.-C. Abadjian, H. N. Tran, G. Kalyuzhny, K. S. Vecchio, Z. G. Specht, S. A. Cortes-Llamas, V. Miranda-Soto, C. van Niekerk, C. E. Moore, A. L. Rheingold, *J. Am. Chem. Soc.* **2011**, *133*, 19024.
[22] H. Junge, N. Marquet, A. Kammer, S. Denurra, M. Bauer, S. Wohlrab, F. Gärtner, M.-M. Pohl, A. Spannenberg, S. Gladiali, M. Beller, *Chem. – A Eur. J.* **2012**, *18*, 12749.
[23] A. Petronilho, M. Rahman, J. A. Woods, H. Al-Sayyed, H. Müller-Bunz, J. M. Don MacElroy, S. Bernhard, M. Albrecht, *Dalton Trans.* **2012**, *41*, 13074.
[24] Z. Yu, F. Li, L. Sun, *Energy Environ. Sci.* **2015**, *8*, 760.
[25] P. Xu, T. Huang, J. Huang, Y. Yan, T. E. Mallouk, *Proc. Natl. Acad. Sci. USA* **2018**, *115*, 6946.
[26] F. Li, K. Fan, B. Xu, E. Gabrielsson, Q. Daniel, L. Li, L. Sun, *J. Am. Chem. Soc.* **2015**, *137*, 9153.
[27] S. Zhang, H. Ye, J. Hua, H. Tian, *EnergyChem* **2019**, *1*, 100015.
[28] D. Primc, M. Bärtsch, D. Barreca, G. Carraro, C. Maccato, C. Sada, M. Niederberger, *Sustain. Energy Fuels* **2017**, *1*, 199.
[29] S. Kment, F. Riboni, S. Pausova, L. Wang, L. Wang, H. Han, Z. Hubicka, J. Krysa, P. Schmuki, R. Zboril, *Chem. Soc. Rev.* **2017**, *46*, 3716.
[30] S. Piskunov, O. Lisovski, J. Begens, D. Bocharov, Y. F. Zhukovskii, M. Wessel, E. Spohr, *J. Phys. Chem. C* **2015**, *119*, 18686.
[31] D. Lebedev, Y. Pineda-Galvan, Y. Tokimaru, A. Fedorov, N. Kaeffer, C. Copéret, Y. Pushkar, *J. Am. Chem. Soc.* **2018**, *140*, 451.
[32] S. Mukhopadhyay, O. Basu, R. Nasani, S. K. Das, *Chem. Commun.* **2020**, *56*, 11735.
[33] S. Lin, Y. Pineda-Galvan, W. A. Maza, C. C. Epley, J. Zhu, M. C. Kessinger, Y. Pushkar, A. J. Morris, *ChemSusChem* **2017**, *10*, 514.
[34] Z. N. Zahran, Y. Tsubonouchi, E. A. Mohamed, M. Yagi, *ChemSusChem* **2019**, *12*, 1775.
[35] Y. Horiuchi, T. Toyao, K. Miyahara, L. Zakary, D. Do Van, Y. Kamata, T.-H. Kim, S. W. Lee, M. Matsuoka, *Chem. Commun.* **2016**, *52*, 5190.
[36] J. Feng, X. Li, Y. Luo, Z. Su, M. Zhong, B. Yu, J. Shi, *Chin. J. Catal.* **2023**, *48*, 127.
[37] J.-B. Tan, G.-R. Li, *J. Mater. Chem. A Mater.* **2020**, *8*, 14326.
[38] C. Wang, J.-L. Wang, W. Lin, *J. Am. Chem. Soc.* **2012**, *134*, 19895.
[39] B. A. Johnson, A. Bhunia, S. Ott, *Dalton Trans.* **2017**, *46*, 1382.
[40] A. Howe, T. Liseev, M. Gil-Sepulcre, C. Gimbert-Suriñach, J. Benet-Buchholz, A. Llobet, S. Ott, *Mater. Adv.* **2022**, *3*, 4227.
[41] R. Ezhov, A. Karbakhsh Ravari, A. Page, Y. Pushkar, *ACS Catal.* **2020**, *10*, 5299.
[42] J. F. Hull, D. Balcells, J. D. Blakemore, C. D. Incarvito, O. Eisenstein, G. W. Brudvig, R. H. Crabtree, *J. Am. Chem. Soc.* **2009**, *131*, 8730.
[43] C. Wang, Z. Xie, K. E. deKrafft, W. Lin, *J. Am. Chem. Soc.* **2011**, *133*, 13445.
[44] J. D. Blakemore, N. D. Schley, D. Balcells, J. F. Hull, G. W. Olack, C. D. Incarvito, O. Eisenstein, G. W. Brudvig, R. H. Crabtree, *J. Am. Chem. Soc.* **2010**, *132*, 16017.
[45] L. Chi, Q. Xu, X. Liang, J. Wang, X. Su, *Small* **2016**, *12*, 1351.
[46] T. Qiu, Z. Liang, W. Guo, H. Tabassum, S. Gao, R. Zou, *ACS Energy Lett.* **2020**, *5*, 520.
[47] D. Wang, Y. Song, J. Cai, L. Wu, Z. Li, *New J. Chem.* **2016**, *40*, 9170.
[48] W. Zhen, J. Ma, G. Lu, *Appl. Catal. B* **2016**, *190*, 12.
[49] Y. Wang, Y. Zhang, Z. Jiang, G. Jiang, Z. Zhao, Q. Wu, Y. Liu, Q. Xu, A. Duan, C. Xu, *Appl. Catal. B* **2016**, *185*, 307.
[50] J.-D. Xiao, Q. Shang, Y. Xiong, Q. Zhang, Y. Luo, S.-H. Yu, H.-L. Jiang, *Angew. Chem., Int. Ed.* **2016**, *55*, 9389.
[51] J. Li, H. Huang, P. Liu, X. Song, D. Mei, Y. Tang, X. Wang, C. Zhong, *J. Catal.* **2019**, *375*, 351.
[52] R. Ezhov, A. K. Ravari, M. Palenik, A. Loomis, D. M. Meira, S. Savikhin, Y. Pushkar, *ChemSusChem* **2023**, *16*, 202202124.
[53] L. Duan, C. M. Araujo, M. S. G. Ahlquist, L. Sun, *Proc. Natl. Acad. Sci. USA* **2012**, *109*, 15584.
[54] Y. Pushkar, Y. Pineda-Galvan, A. K. Ravari, T. Otroshchenko, D. A. Hartzler, *J. Am. Chem. Soc.* **2018**, *140*, 13538.
[55] Y. Umena, K. Kawakami, J.-R. Shen, N. Kamiya, *Nature* **2011**, *473*, 55.
[56] K. M. Davis, B. T. Sullivan, M. C. Palenik, L. Yan, V. Purohit, G. Robison, I. Kosheleva, R. W. Henning, G. T. Seidler, Y. Pushkar, *Phys. Rev.* **2018**, *8*, 041014.
[57] M. A. Hoque, A. D. Chowdhury, S. Maji, J. Benet-Buchholz, M. Z. Ertem, C. Gimbert-Suriñach, G. K. Lahiri, A. Llobet, *Inorg. Chem.* **2021**, *60*, 5791.
[58] S. Lin, A. K. Ravari, J. Zhu, P. M. Usov, M. Cai, S. R. Ahrenholtz, Y. Pushkar, A. J. Morris, *ChemSusChem* **2018**, *11*, 464.

[59] L. Shi, T. Wang, H. Zhang, K. Chang, X. Meng, H. Liu, J. Ye, *Adv. Sci.* **2015**, *2*, 1500006.
[60] J. Joseph, S. Iftekhar, V. Srivastava, Z. Fallah, E. N. Zare, M. Sillanpää, *Chemosphere* **2021**, *284*, 131171.
[61] Y. Zhang, J. Li, X. Yang, P. Zhang, J. Pang, B. Li, H.-C. Zhou, *Chem. Commun.* **2019**, *55*, 2023.
[62] G. Bury, Y. Pushkar, *Catalysts* **2022**, *12*, 863.
[63] D. Moonshiram, Y. Pineda-Galvan, D. Erdman, M. Palenik, R. Zong, R. Thummel, Y. Pushkar, *J. Am. Chem. Soc.* **2016**, *138*, 15605.
[64] A. K. Ravari, G. Zhu, R. Ezhov, Y. Pineda-Galvan, A. Page, W. Weinschenk, L. Yan, Y. Pushkar, *J. Am. Chem. Soc.* **2020**, *142*, 884.
[65] M. Yagi, S. Tajima, M. Komi, H. Yamazaki, *Dalton Trans.* **2011**, *40*, 3802.
[66] H. Chevreau, T. Devic, F. Salles, G. Maurin, N. Stock, C. Serre, *Angew. Chem., Int. Ed.* **2013**, *52*, 5056.
[67] R. R. R. Prasad, C. Pleass, A. L. Rigg, D. B. Cordes, M. M. Lozinska, V. M. Georgieva, F. Hoffmann, A. M. Z. Slawin, P. A. Wright, *CrystEngComm* **2021**, *23*, 804.
[68] L. Li, B. Das, A. Rahaman, A. Shatskiy, F. Ye, P. Cheng, C. Yuan, Z. Yang, O. Verho, M. D. Kärkäs, J. Dutta, T.-C. Weng, B. Åkermark, *Dalton Trans.* **2022**, *51*, 7957.
[69] M. M. Al-Hinaai, H. H. Kyaw, S. H. Al-Harthi, E. A. Khudaish, *Sens. Actuators B Chem.* **2018**, *257*, 460.
[70] Y. Zhang, W. Huo, H.-Y. Zhang, J. Zhao, *RSC. Adv.* **2017**, *7*, 47261.
[71] Y. Mei, T.-T. Li, J. Qian, H. Li, Y.-Q. Zheng, *J. Mater. Sci.* **2020**, *55*, 12864.
[72] Z. Zhou, S. Wu, C. Xiao, L. Li, W. Shao, H. Ding, L. Wen, X. Li, *Dalton Trans.* **2019**, *48*, 15151.
[73] X. Bu, G. Wang, Y. Tian, *Nanoscale* **2017**, *9*, 17513.
[74] M. Szkoda, K. Trzciński, M. Łapiński, A. Lisowska-Oleksiak, *Electrocatalysis* **2020**, *11*, 111.
[75] Y. Horiuchi, T. Toyao, K. Miyahara, L. Zakary, D. Do Van, Y. Kamata, T.-H. Kim, S. W. Lee, M. Matsuoka, *Chem. Commun.* **2016**, *52*, 5190.
[76] W.-H. Cheng, M. H. Richter, M. M. May, J. Ohlmann, D. Lackner, F. Dimroth, T. Hannappel, H. A. Atwater, H.-J. Lewerenz, *ACS Energy Lett.* **2018**, *3*, 1795.
[77] H. H. Do, D. L. T. Nguyen, X. C. Nguyen, T.-H. Le, T. P. Nguyen, Q. T. Trinh, S. H. Ahn, D.-V. N. Vo, S. Y. Kim, Q. Van Le, *Arabian J. Chem.* **2020**, *13*, 3653.
[78] H. Eidsvåg, S. Bentouba, P. Vajeeston, S. Yohi, D. Velauthapillai, *Molecules* **2021**, *26*, 1687.
[79] C. Wang, K. E. deKrafft, W. Lin, *J. Am. Chem. Soc.* **2012**, *134*, 7211.
[80] J. S. DuChene, G. Tagliabue, A. J. Welch, X. Li, W.-H. Cheng, H. A. Atwater, *Nano Lett.* **2020**, *20*, 2348.
[81] C. Yavuz, S. Erten-Ela, *J. Alloys Compd.* **2022**, *908*, 164584.
[82] Y. K. Sofi'i, E. Siswanto, T. U. Winarto, I. N. G. Wardana, *Int. J. Hydrogen Energy* **2020**, *45*, 22613.
[83] L. S. Xie, G. Skorupskii, M. Dincă, *Chem. Rev.* **2020**, *120*, 8536.